Density-functional study of perovskite-type hydride $LiNiH_3$ and its synthesis: Mechanism for formation of metallic perovskite

Shigeyuki Takagi,[1] Hiroyuki Saitoh,[2] Naruki Endo,[2] Ryutaro Sato,[1] Tamio Ikeshoji,[1] Motoaki Matsuo,[1] Kazutoshi Miwa,[3] Katsutoshi Aoki,[1] and Shin-ichi Orimo[1,4,*]

[1]*Institute for Materials Research, Tohoku University, Sendai 980-8577, Japan*
[2]*Quantum Beam Science Directorate, Japan Atomic Energy Agency, Hyogo 679-5148, Japan*
[3]*Toyota Central Research and Development Laboratories, Inc., Nagakute 480-1192, Japan*
[4]*WPI-Advanced Institute for Materials Research, Tohoku University, Sendai 980-8577, Japan*

(Received 23 January 2013; published 21 March 2013)

A metallic perovskite-type hydride $LiNiH_3$ was synthesized based on first-principles prediction. We theoretically examined its electronic structure and found that half of the Ni-H derived antibonding states are occupied and that the modest thermodynamic stability depends on a delicate balance between (i) destabilization and (ii) alleviation of compression frustration in corner-sharing octahedra, both of which arise from occupation of antibonding states. Through density-functional analyses of the electronic structure and lattice instability extending over $LiTH_3$ series (T = Fe, Co, Ni, and Cu), we showed that the balance is in fact reflected in their thermodynamic stability.

DOI: 10.1103/PhysRevB.87.125134 PACS number(s): 71.20.Be, 71.20.Dg, 63.20.D−, 61.05.cp

I. INTRODUCTION

Perovskites ABX_3 have attracted considerable interest for many years owing to a variety of physical properties mostly related to a specific structural motif and resulting electronic structure. One remarkable example of this is the family of perovskite oxides, of which an enormous number of compounds have been synthesized to date. They typically have a structure distorted from that of an ideal perovskite and often show a ferroelectricity that depends on a delicate balance between covalent interaction, long-range Coulomb forces, and short-range ionic repulsions.[1] More generally, instabilities in perovskites can often be understood in terms of a so-called tolerance factor that describes the competition between preferred A-X and B-X bond lengths. In addition to ferroelectricity, their solid solutions frequently exhibit an electromechanical response related to polarization rotation near morphotropic phase boundaries.[2] Furthermore, most high-temperature superconducting oxides, such as Ba-La-Cu-O and Hg-Ba-Ca-Cu-O systems,[3,4] have a structure associated with perovskite.

In contrast, only a few perovskites are known in the hydrides, reflecting the fact that there are only two possible combinations within a ternary perovskite-type hydride (i.e., $A^+B^{2+}H_3^-$ and $A^{2+}B^+H_3^-$). In fact, many of the perovskite-type hydrides consist of monovalent alkali and divalent alkaline earth metal elements, such as $NaMgH_3$, $KMgH_3$, $SrLiH_3$, and $BaLiH_3$,[5–10] and are insulators with a substantial band gap.[11,12] These hydrides are of importance in terms of hydrogen storage due to their high density of hydrogen.

Aside from these ionic compounds, another group of the perovskite-type hydrides exists, which does not show a band gap at the Fermi level: this group includes $CaCoH_3$, $CaNiH_3$, $SrPdH_3$, $EuPdH_3$, and $YbPdH_3$.[7,11,13–16] In addition to the specific structure, the metallic electronic structure implies that they are the potential candidates for superconducting materials, and some have been studied from this viewpoint,[17–20] although no superconducting perovskites have been found to date. It can be readily seen, then, that the many varieties and compositions of materials in this group deserve further exploration. Related to this, the metallic electronic structure strongly suggests a certain degree of chemical flexibility in contrast to the ionic perovskite-type hydrides, while all the compounds found consist of only an alkaline earth or a rare-earth metal element on the A site and a transition-metal element on the B site.

In this context, the possible synthesis of a metallic perovskite-type hydride $LiNiH_3$, which contains an alkali metal element on the A site and a transition metal element on the B site, was theoretically and experimentally examined. We investigated the electronic structure and elucidated the mechanism for the formation of metallic perovskite-type hydride. In addition, through the density-functional investigation for the series of perovskite-type hydrides $LiTH_3$ (T = Fe, Co, Ni, and Cu), we found a way to synthesize metallic perovskite-type hydrides.

II. APPROACH

A. First-principles calculations

The possible synthesis of perovskite-type hydride $LiNiH_3$, and the electronic structure, lattice instability, and energetics for the series of perovskite-type hydrides $LiTH_3$ (T = Fe, Co, Ni, and Cu) were investigated using first-principles calculations based on density-functional theory (DFT). We performed the structural optimization of $LiNiH_3$ using a $2 \times 2 \times 2$ supercell (40 atoms), which has an even number of NiH_6 octahedra along the [001], [011], and [111] directions [cf. Fig. 4(a)] and therefore can accommodate the various Glazer tilt patterns of the corner-sharing octahedra[21] in the same manner as the perovskite oxides.[22–24] The five-atom primitive cells of the ideal cubic perovskite structure were used for the calculation of the series of $LiTH_3$ to see the lattice instability, where only the lattice constants were optimized within the cubic lattice and with fixed internal coordinates of constituents.

These calculations were performed using a plane-wave basis and projector augmented wave method[25,26] within the

generalized gradient approximation with the exchange and correlation functional of Perdew, Burke, and Ernzerhof,[27] as implemented in the Vienna Ab-Initio Simulation Package (VASP).[28,29] Well-converged plane-wave basis sets with cutoff energies of 800 and 7200 eV for wave function and charge density, respectively, were employed. The Brillouin-zone sampling was performed using the special k-points method[30] with an $8 \times 8 \times 8$ mesh, and the results were also converged with respect to the sampling. The phonon calculations were performed using the PHONOPY code,[31] based on a supercell approach,[32] with force constants obtained from VASP calculations in a $3 \times 3 \times 3$ supercell (135 atoms) with the cutoff energies of 400 and 3600 eV for wave fuction and charge density, respectively, and with a $4 \times 4 \times 4$ k-point mesh.

B. Experiment

High-purity Ni powder (99.5%, CERAC) was mixed with LiH (99.4%, Alfa Aesar) at a molar ratio of 1:2 by mechanical milling at 400 rpm for 2 h under 0.1 MPa Ar atmosphere (note that the excess of LiH was supplied to compensate for LiH dissolution within the high-pressure cell). Following this, hydrogenation was conducted using a multianvil high-pressure apparatus under 6 GPa at 873 K for 3 h. A sample, recovered at ambient pressure and temperature, was characterized by white synchrotron-radiation x-ray-diffraction (SR-XRD) measurement at beamline BL14B1 in SPring-8.[33] We employed the energy-dispersive x-ray-diffraction method. Details of our experimental apparatus and technique are described elsewhere.[34–38]

III. RESULTS

A. $LiNiH_3$

1. *First-principles prediction and synthesis*

The structural optimization provided a cubic lattice with a lattice parameter of 6.50 Å (i.e., 3.25 Å for the five-atom primitive unit cell). We did not find any atomic displacements from the ideal perovskite structure.

We then estimated the thermodynamic stability of this perovskite-type hydride. The standard heats of formation of $LiNiH_3$ and its related decomposed product, LiH, were calculated by comparing their total energies with those of the elements Li and Ni in bulk metallic form and of the H_2 molecule. The finite-temperature effect was taken into account within the harmonic approximation, and the zero-point energy (ZPE) contributions were included. The results are listed in Table I. Here, the value of -81 kJ/mol for LiH is in reasonable agreement with the experimentally reported value of -91 kJ/mol.[39] We obtained a standard heat of formation of -118 kJ/mol for the perovskite-type hydride $LiNiH_3$.

TABLE I. DFT based standard heat of formation ΔH_f°(DFT) expressed in kJ/mol. Experimental values are given as ΔH_f°(Exp).[39]

Compound	ΔH_f°(DFT)	ΔH_f°(Exp)
LiH	-81	-91
$LiNiH_3$	-119	–

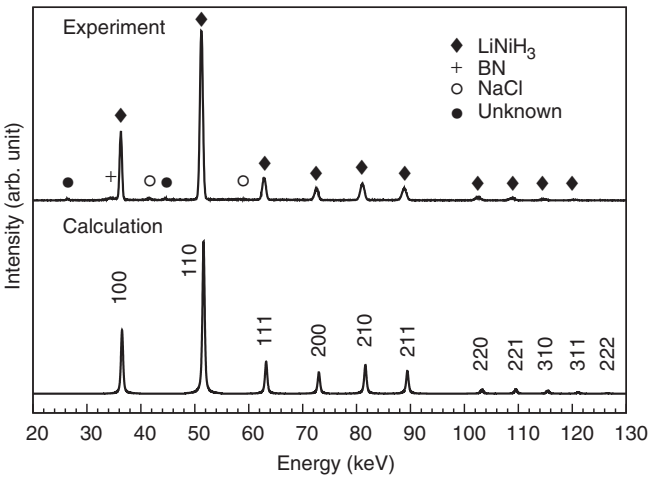

FIG. 1. Experimentally and theoretically obtained XRD profiles for $LiNiH_3$. The top panel shows the white SR-XRD profile of a hydrogenated sample, taken at ambient pressure and temperature, and the bottom shows a simulated pattern of optimized $LiNiH_3$ obtained from the DFT calculation (note that the simulated energy-dispersive profile was converted from the simulated angle-dispersive data, taking into account the energy spectrum of the incident x-ray and x-ray absorption). $LiNiH_3$ is denoted by closed diamonds, BN by crosses, NaCl by open circles, and the unidentified phase by closed circles.

Based on these results, the enthalpy change of the reaction, $LiH + Ni + H_2 \rightarrow LiNiH_3$, was estimated to be -38 kJ/mol H_2, which is comparable to that of $LaNi_5$ hydrogenation (-32 kJ/mol H_2)[40] and indicates a possible synthesis of $LiNiH_3$ via this reaction. Using a calculated entropy change of -112 J/mol H_2 K, the equilibrium pressure at 873 K was estimated to be 382 MPa and the decomposition temperature at ambient pressure was 338 K.

In order to verify our first-principles prediction, a high-pressure and high-temperature technique was used to synthesize $LiNiH_3$. The obtained sample has a dark gray color with a slight metallic lusting, implying the electronic conduction. The energy-dispersive SR-XRD profile for a hydrogenated sample taken at ambient pressure and temperature is depicted in Fig. 1. Here, the Bragg peaks are well indexed to a simple-cubic lattice with a lattice parameter of 3.266 ± 0.001 Å, although the sample contains a small amount of impurities (BN and NaCl) from the high-pressure cell. Figure 1 also shows a DFT-derived simulated pattern of a perovskite-type hydride $LiNiH_3$. As can be seen, the two profiles are practically identical, indicating a successful synthesis of the perovskite-type hydride $LiNiH_3$.

2. *Electronic structure*

We examined the electronic structure of perovskite-type hydride $LiNiH_3$ to understand the underlying physics. The electronic band structure and corresponding density of states (DOS) with H 1s, Ni 4s, and Ni 3d projections are depicted in Figs. 2 and 3, respectively. We took into account the spin polarization and found that a non-spin-polarized state is energetically the most stable.

In an octahedral ligand field, the three H 1s states form a linear combination of irreducible representations, $a_{1g} + e_g$, while the Ni 3d and 4s states compose a linear combination,

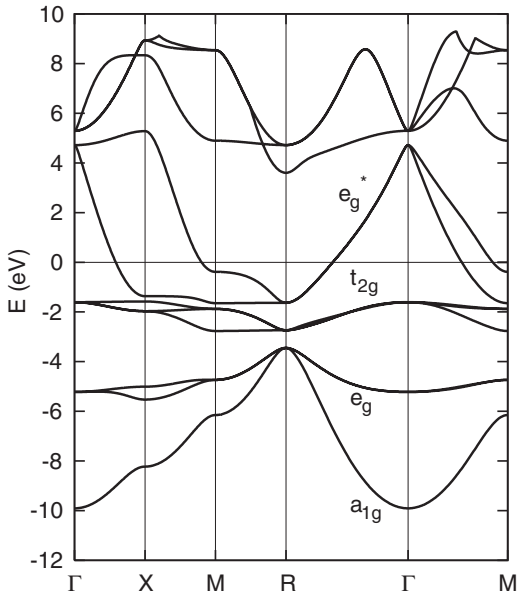

FIG. 2. Electronic band structure for the five-atom primitive cell of fully relaxed perovskite-type hydride $LiNiH_3$ along the high-symmetry line in the Brillouin zone. The energy zero is set at the valence-band maximum.

$a_{1g} + e_g + t_{2g}$. They form three formally bonding ($a_{1g} + e_g$), three formally antibonding ($a_{1g}^* + e_g^*$), and three formally nonbonding (t_{2g}) states, as can be clearly seen in the electronic structure described below.

The three lowest branches, extending from −10 to −3.5 eV, are the formally bonding a_{1g} and e_g manifolds, as may be seen from the H 1s, Ni 4s, and Ni 3d characters in the corresponding DOS. The formally nonbonding t_{2g} states provide a sharp DOS from −2.9 to −1.7 eV separated from the formally antibonding e_g^* states between −1.7 and 5 eV by a very narrow ligand-field gap at −1.7 eV. The narrowness of this gap is a consequence of the corner-sharing structure of NiH_6 octahedra, which restricts the Ni-H bond length to 1.63 Å (cf. 1.54–1.57 Å

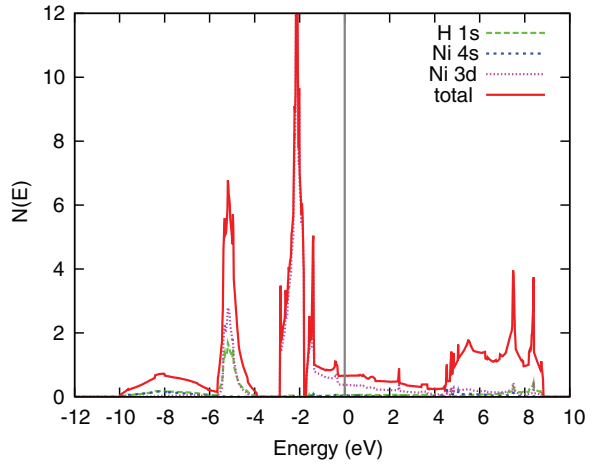

FIG. 3. (Color online) Total electronic DOS and H 1s, Ni 4s, and Ni 3d projections for the five-atom primitive cell of fully relaxed perovskite-type hydride $LiNiH_3$. The energy zero is set at the valence-band maximum.

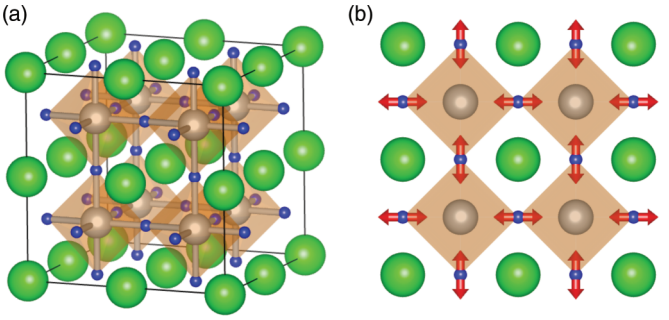

FIG. 4. (Color online) (a) Structure of the 40-atom $LiNiH_3$ supercell and (b) schematic depiction of compression frustration in corner-sharing octahedra. Hydrogen atoms are shown by small (blue), lithium by large (light green), and nickel by medium (silver) spheres, respectively. The Ni-H bonds and NiH_6 octahedra are shown. Owing to the corner-sharing structure, each H atom participates in the formation of two Ni-H bonds pointing in opposite directions, giving rise to compression frustration in the octahedra.

in each separate NiH_4 unit of complex hydride Mg_2NiH_4),[41] thereby suppressing the ligand-field splitting. As the Fermi level falls within the antibonding e_g^* states, the valence bands are composed of a_{1g} (two electron), e_g (four electron), t_{2g} (six electron), and half filled antibonding e_g^* states (two electron).

It is significant that, unlike in ionic perovskite-type hydrides, half of the Ni-H derived antibonding states are occupied by two electrons; this is the key to understanding the mechanism of formation of metallic perovskite, and we now discuss the effect of antibonding occupation on the thermodynamic stability.

Such antibonding occupations normally lead to destabilization, which competes with the formation of hydride. At the same time, antibonding occupations weaken the Ni-H chemical bonding, which in turn contributes to a stabilization in the formation of hydride, as the weakened bonding alleviates the compression frustration in the corner-sharing octahedra [cf. Fig. 4(b)]. Thus, the modest thermodynamic stability in the metallic perovskite-type hydride $LiNiH_3$ most likely depends on the delicate balance of two competing effects: (i) destabilization and (ii) alleviation of frustration, both of which arise from the occupation of antibonding e_g^* states. The very narrow ligand-field gap also helps reduce the destabilization, as additional occupations above the nonbonding t_{2g} states will lead to only slight destabilization.

To better understand these mechanisms, it would be beneficial to investigate the perovskite-type hydride series $LiTH_3$ (T = Fe, Co, Ni, and Cu). The motivation for this choice is that the series has increasing electron count with increasing atomic number of the transition-metal element T, which is expected to provide increasing occupation number of antibonding e_g^* states. It therefore is helpful to look at the effects of destabilization and frustration alleviation on the thermodynamic stability.

With this in mind, we first calculated the electronic structures for the $LiTH_3$ series in order to evaluate the occupation numbers of the antibonding e_g^* states, $n_{e_g^*}$, associated directly with destabilization, after which we calculated the phonon dispersion curves of $LiTH_3$ with the ideal perovskite structure

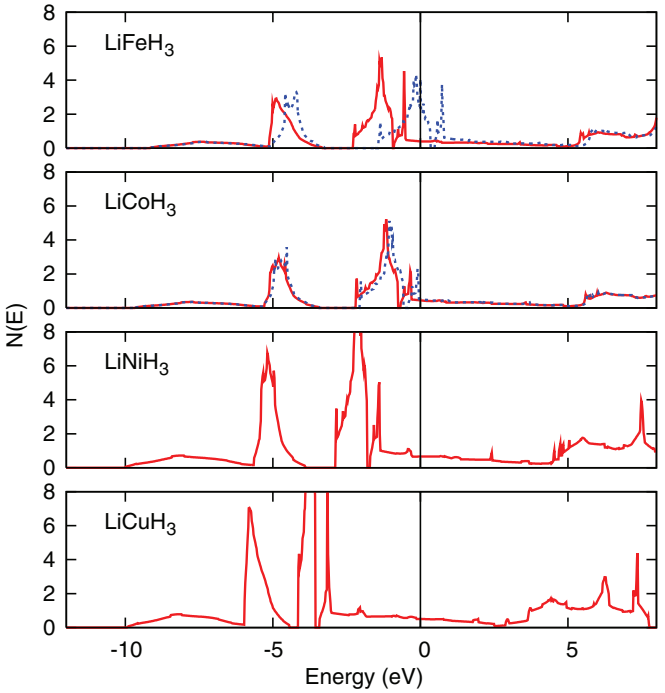

FIG. 5. (Color online) Electronic DOS of LiTH$_3$ (T = Fe, Co, Ni, and Cu) with the ideal perovskite structure. The (red) solid lines and (blue) dashed lines denote the majority- (total) and minority-spin DOS, respectively. The valence-band maxima are taken as the energy zeros.

in order to examine the lattice instability associated with frustration alleviation.

B. LiTH$_3$ (T = Fe, Co, Ni, and Cu)

1. Occupation number of antibonding e_g^* state

Figure 5 shows the electronic densities of states of LiTH$_3$. The ferromagnetic state is the most stable for LiFeH$_3$ and LiCoH$_3$, while the ground states for LiNiH$_3$ and LiCuH$_3$ are nonmagnetic. The calculated magnetic moments for LiFeH$_3$ and LiCoH$_3$ are 2.0 and 0.2 μ_B per formula unit, respectively.

We evaluated the occupation numbers of the antibonding states $n_{e_g^*}$ from these densities of states, and the results are listed in Table II and plotted in Fig. 7. As expected from the increase in electron count, the occupation number $n_{e_g^*}$ increases when going from Co to Cu, as can be seen in Fig. 7, but is nearly identical in LiFeH$_3$ and LiCoH$_3$; this leads to the largest destabilization occurring in LiCuH$_3$, followed by LiNiH$_3$, LiCoH$_3$, and LiFeH$_3$.

TABLE II. Occupation number of antibonding e_g^* states $n_{e_g^*}$, imaginary phonon frequency at R point Im($\omega(R)$) in cm^{-1}, and formation energy ΔE_f in kJ/mol. The finite-temperature effect and ZPE contributions are not taken into account.

Compound	$n_{e_g^*}$	Im($\omega(R)$)	ΔE_f
LiFeH$_3$	1.0	210	−34
LiCoH$_3$	1.0	28	−92
LiNiH$_3$	2.0	0	−119
LiCuH$_3$	3.0	0	−28

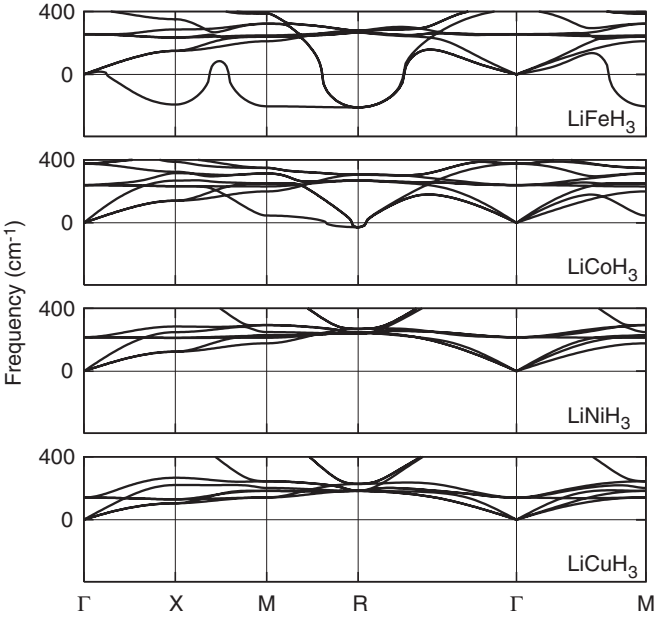

FIG. 6. Phonon dispersion curves for LiTH$_3$ (T = Fe, Co, Ni, and Cu) with the ideal perovskite structure along the high-symmetry line in the Brillouin zone.

2. Lattice instability

The phonon dispersion curves are shown in Fig. 6 . It can be seen that, while LiNiH$_3$ and LiCuH$_3$ have no imaginary frequency, LiFeH$_3$ and LiCoH$_3$ show lattice instabilities at the zone boundary, particularly at the R point. This is reminiscent of octahedral tilt instabilities found in low tolerance factor perovskites, such as NaMgH$_3$[12] (note that, in such perovskites, the A-site ion has more room than the B-site ion, which leads to octahedral tilting), and can probably be understood in terms of the T-H bond strength; i.e., if a strong T-H bond is present, the T on the B site will be strongly bound to the center of the H cage and behave as if it does not have room to be

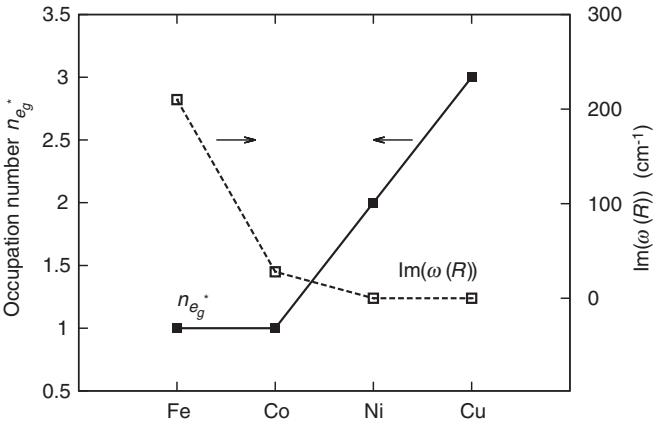

FIG. 7. Occupation number of antibonding states $n_{e_g^*}$ and imaginary phonon frequency at R-point Im($\omega(R)$) for LiTH$_3$ (T = Fe, Co, Ni, and Cu). $n_{e_g^*}$ is denoted by open squares and Im($\omega(R)$) by closed squares. The solid and dashed lines serve as visual guides.

off-center, yielding the lattice instability seen in low tolerance factor perovskites. This is the case for $LiFeH_3$, which has a small occupation number of antibonding e_g^* states relative to both $LiNiH_3$ and $LiCuH_3$ and, therefore, has a stronger T-H bond. $LiCoH_3$ also shows similar instabilities, but its imaginary frequencies are smaller than those of $LiFeH_3$. The imaginary phonon frequencies at the R point are summarized in Table II and plotted in Fig. 7. It can be seen from these that frustration is the strongest in $LiFeH_3$, followed by $LiCoH_3$, $LiNiH_3$, and $LiCuH_3$.

3. *Thermodynamic stability*

The trends seen in Fig. 7 are clearly reflected in the formation energies listed in Table II. While the formation energies for $LiFeH_3$ and $LiCuH_3$ are rather small, reflecting, respectively, a large imaginary frequency $\omega(R)$ and occupation number $n_{e_g^*}$, $LiCoH_3$ and $LiNiH_3$ have modest thermodynamic stability. It should be noted that the atomic relaxations in order to freeze the soft modes do not make a significant contribution to the trends seen here. The fully relaxed structures and their resulting standard heats of formations are given as supplemental material.[42]

IV. SUMMARY AND DISCUSSION

Based on first-principles prediction, we synthesized a metallic perovskite-type hydride $LiNiH_3$. In examining the electronic structure of this compound, we found that half of the Ni-H derived antibonding states are occupied, forming the metallic electronic structure. We also found that a delicate balance of (i) destabilization and (ii) alleviation of compression frustration in corner-sharing octahedra, both of which arise from the antibonding occupation, dominates the thermodynamic stability. Based on the investigation of the $LiTH_3$ series (T = Fe, Co, Ni, and Cu), we demonstrated that competition between (i) destabilization and (ii) frustration alleviation is in fact reflected in their thermodynamic stability.

With the exception of $LiNiH_3$, it may be difficult to synthesize the metallic perovskite-type hydrides studied here, owing to their low thermodynamic stability relative to LiH (cf. Tables I and II). One way to overcome this difficulty would be to expand the perovskite lattice by Li-substituting elements with larger ion sizes, such as Na, K, and Rb, which weakens the T-H chemical bonding without additional antibonding occupation, thereby suppressing any lattice instability related to compression frustration of the corner-sharing octahedra. From a geometric point of view, such a substitution would correspond to a reduction in the competition between preferred A-H and B-H bond length, in other words, adjustment of the low tolerance factor toward unity. This idea is supported by experimental results obtained for the synthesis of $CaCoH_3$ and $CaNiH_3$ under mild conditions[11,13] (note that Ca^{2+} has a much larger ionic radius than Li^+).[43] Additionally, the two hydrides occur in the ideal cubic perovskite structure,[7] which would be understood in terms of less competition between preferred A-H and B-H bond length. Furthermore, the fact that all the metallic perovskite-type hydrides reported have ideal perovskite-related structure, at least cubic lattice,[7] would also support the present discussion. In this regard, it may be of interest to see if ATH_3 (A = Na, K, Rb, T = Fe, Co, Ni) can be synthesized. All these are dense metallic hydrogen-rich compounds, which have been regarded as candidates for superconductors.[44,45] Thus the proposed mechanism would be helpful in finding compositions with superconductivity amenable to synthesis.

ACKNOWLEDGMENT

We are grateful to Dr. T. Sato of Tohoku University and Dr. D. Y. Kim of Carnegie Institution of Washington for helpful discussions, and to Ms. N. Warifune and Ms. H. Ohmiya for the technical support they provided. This research was performed under the Shared Use Program of Japan Atomic Energy Agency (JAEA) Facilities. Synchrotron-radiation experiments were performed at the JAEA beamline in SPring-8 (Proposal No. 2012B3620). This work was funded by "Funding Program for Next Generation World-Leading Researchers" (Grant No. GR008). Figure 4 was produced using the VESTA program.[46]

*orimo@imr.tohoku.ac.jp

[1] R. E. Cohen, Nature (London) **358**, 136 (1992).
[2] H. Fu and R. E. Cohen, Nature (London) **403**, 281 (2000).
[3] J. G. Bednorz and K. A. Müller, Z. Phys. B **64**, 189 (1986).
[4] A. Schilling, M. Cantoni, J. D. Guo, and H. R. Ott, Nature (London) **363**, 56 (1993).
[5] E. Rönnebro, D. Noréus, K. Kadir, A. Reiser, and B. Bogdanovic, J. Alloys Compd. **299**, 101 (2000).
[6] K. Ikeda, S. Kato, Y. Shinzato, N. Okuda, Y. Nakamori, A. Kitano, H. Yukawa, M. Morinaga, and S. Orimo, J. Alloys Compd. **446-447**, 162 (2007).
[7] K. Ikeda, T. Sato, and S. Orimo, Int. J. Mat. Res. **99**, 5 (2008).
[8] H. H. Park, M. Pezat, B. Darriet, and P. Hagenmuller, Rev. Chim. Miner. **24**, 525 (1987).
[9] C. E. Messer, J. C. Eastman, R. G. Mers, and A. J. Maeland, Inorg. Chem. **3**, 776 (1964).
[10] A. J. Maeland and A. F. Andresen, J. Chem. Phys. **48**, 4660 (1968).
[11] T. Sato, D. Noréus, H. Takeshita, and U. Häussermann, J. Solid State Chem. **178**, 3381 (2005).
[12] M. Fornari, A. Subedi, and D. J. Singh, Phys. Rev. B **76**, 214118 (2007).
[13] K. Ikeda, S. Kato, K. Ohoyama, Y. Nakamori, H. Takeshita, and S. Orimo, Scr. Mater. **55**, 827 (2006).
[14] W. Bronger and G. Ridder, J. Alloys Compd. **210**, 53 (1994).
[15] H. Khlmann, H. E. Fischer, and K. Yvon, Inorg. Chem. **40**, 2608 (2001).
[16] K. Ensslen, E. Bucher, and H. Oesterreicher, J. Less-Common Met. **92**, 343 (1983).
[17] E. Orgaz and M. Gupta, J. Alloys Compd. **231**, 147 (1995).
[18] E. Orgaz, V. Mazel, and M. Gupta, Phys. Rev. B **54**, 16124 (1996).
[19] E. Orgaz, V. Mazel, and M. Gupta, J. Alloys Compd. **254**, 330 (1997).
[20] S. Ayukawa, K. Ikeda, M. Kato, T. Noji, S. Orimo, and Y. Koike, J. Phys. Soc. Jpn. **81**, 034704 (2012).

[21] A. M. Glazer, Acta Crystallogr. B **28**, 3384 (1972).
[22] S. Takagi, A. Subedi, D. J. Singh, and V. R. Cooper, Phys. Rev. B **81**, 134106 (2010).
[23] S. Takagi, A. Subedi, V. R. Cooper, and D. J. Singh, Phys. Rev. B **82**, 134108 (2010).
[24] S. Takagi, V. R. Cooper, and D. J. Singh, Phys. Rev. B **83**, 115130 (2011).
[25] P. E. Blöchl, Phys. Rev. B **50**, 17953 (1994).
[26] G. Kresse and D. Joubert, Phys. Rev. B **59**, 1758 (1999).
[27] J. P. Perdew, K. Burke, and M. Ernzerhof, Phys. Rev. Lett. **77**, 3865 (1996).
[28] G. Kresse and J. Hafner, Phys. Rev. B **47**, 558 (1993).
[29] G. Kresse and J. Furthmüller, Phys. Rev. B **54**, 11169 (1996).
[30] H. J. Monkhorst and J. D. Pack, Phys. Rev. B **13**, 5188 (1976).
[31] A. Togo, F. Oba, and I. Tanaka, Phys. Rev. B **78**, 134106 (2008); the code is taken from http://phonopy.sourceforge.net/.
[32] K. Parlinski, Z. Q. Li, and Y. Kawazoe, Phys. Rev. Lett. **78**, 4063 (1997).
[33] W. Utsumi, K. Funakoshi, Y. Katayama, M. Yamakata, T. Okada, and O. Shimomura, J. Phys.: Condens. Matter **14**, 10497 (2002).
[34] H. Saitoh, A. Machida, Y. Katayama, and K. Aoki, Appl. Phys. Lett. **93**, 151918 (2008).
[35] H. Saitoh, A. Machida, Y. Katayama, and K. Aoki, Appl. Phys. Lett. **94**, 151915 (2009).
[36] H. Saitoh, Y. Okajima, Y. Yoneda, A. Machida, D. Kawana, T. Watanuki, Y. Katayama, and K. Aoki, J. Alloys Compd. **496**, L25 (2010).
[37] N. Endo, H. Saitoh, A. Machida, Y. Katayama, and K. Aoki, J. Alloys Compd. **546**, 270 (2013).
[38] R. Sato, H. Saitoh, N. Endo, S. Takagi, M. Matsuo, K. Aoki, and S. Orimo, Appl. Phys. Lett. **102**, 091901 (2013).
[39] F. E. Pretzel, G. N. Rupert, C. L. Mader, E. K. Storms, G. V. Gritton, and C. C. Rushing, J. Phys. Chem. Solids **16**, 10 (1960).
[40] H. H. V. Mal, K. H. J. Buschow, and A. R. Miedema, J. Less-Common Met. **35**, 65 (1974).
[41] K. Yvon, CHIMIA **52**, 613 (1998).
[42] See Supplemental Material at http://link.aps.org/supplemental/10.1103/PhysRevB.87.125134 for data on the fully relaxed crystal structures of $LiFeH_3$ and $LiFeH_3$, and their standard heat of formations.
[43] R. D. Shannon, Acta. Crystallogr. A: Cryst. Phys., Diffr., Theor. Gen. Crystallogr. **32**, 751 (1976).
[44] N. W. Ashcroft, Phys. Rev. Lett. **32**, 187002 (2004).
[45] M. I. Eremets, I. A. Trojan, S. A. Medvedev, J. S. Tse, and Y. Yao, Science **319**, 1506 (2008).
[46] K. Momma and F. Izumi, J. Appl. Crystallogr. **44**, 1272 (2011); the code is taken from http://jp-minerals.org/vesta/en/.